Reducing Soot Emissions in a Diesel Series Hybrid Electric Vehicle Using a Power Rate Constraint Map

Youngki Kim, *Member, IEEE*, Ashwin Salvi, Anna G. Stefanopoulou, *Fellow, IEEE*, and Tulga Ersal

Abstract—This paper considers a diesel series hybrid electric vehicle (SHEV) and proposes the utilization of an engine–generator power rate constraint map to reduce soot emissions without a significant compromise in fuel economy. Specifically, model predictive control (MPC) is used to split the vehicle power demand between the engine–generator unit and the battery. To achieve a reduction in soot, the engine–generator power rate is constrained. Unlike existing strategies, the power rate limit is not a fixed value but varies, depending on the power level, resulting in a map. This constraint map is designed by formulating the soot emission reduction problem as an optimization problem, which is solved through a three-step offline discrete optimization process. The optimization relies on a quasi-static soot emissions map that captures the trends, even during transients, but underestimates the magnitudes. Therefore, to evaluate the performance of the MPC-based power management with the power rate constraint map, experiments are conducted through an engine-in-the-loop simulation framework. Experimental results show that compared with a constant power rate constraint, soot emissions can be reduced by 44.5% while compromising fuel economy by only 0.3% through the proposed approach. As a tradeoff, the ampere-hour (Ah) processed in the battery, which is a variable that has been shown to correlate with battery capacity loss, increases by 5.5%.

Index Terms—Diesel engines, discrete optimization, model predictive control (MPC), power management, series hybrid electric vehicles (SHEVs), soot emissions.

I. INTRODUCTION

DIESEL engines are favored in heavy-duty commercial and military applications as they have high performance in terms of fuel economy, torque at low speed, and power density [1]. However, their soot emissions lead to environmental concerns in commercial applications, as well as survivability concerns in military applications due to visual signature. Aggressive transients worsen soot emissions [2] because of a turbocharger lag, which corresponds to the slow air-path dynamics of a diesel engine with a time constant of a few seconds [3].

One approach to reduce soot emissions is to leverage hybrid powertrain technology. This technology has been successfully deployed in some passenger vehicles, improving fuel economy and reducing tailpipe emissions [4], [5], and vehicles with diesel engines can benefit from hybridization as well [6].

Among the various topologies for vehicle hybridization, such as series [7], [8], parallel [9], [10], and power-split [11], [12], this paper focuses on a series hybrid electric architecture with a military context in mind. The series hybrid electric technology is considered in military vehicles due to stringent requirements for silent watch, increased mobility, enhanced functionality for on-board power, improved power-export capabilities, and the potential for minimal visual signature. In addition, compared with other configurations, the series configuration offers greater flexibility in vehicle design such as the V-shaped hull to maximize crew survivability during blast events [13].

Within the context of series hybrid electric vehicles (SHEVs), different power management strategies (PMSs) have been developed in the literature to successfully alleviate the tradeoff, associated with rapid power changes, between fuel economy and soot emissions. For example, Filipi and Kim [7] proposed a modulated battery state-of-charge (SOC) control using a proportional–integral (PI) feedback control. Konev *et al.* [14] and Kim *et al.* [15] used low-pass filtering to split the power demand. Although these methods result in smooth engine operations, the engine power rate is not strictly considered as a constraint for engine operations. Di Cairano *et al.* explicitly handled a fixed power rate constraint by applying model predictive control (MPC) [16]. They also showed that the MPC-based PMS performance was comparable to that of the dynamic programming in terms of fuel economy. However, the influence of smooth engine operations on emissions reduction has not been investigated.

In this paper, a methodology to design a *power rate constraint map* for an engine–generator of an SHEV is proposed to reduce soot emissions. Unlike the approach described in [16], the maximum engine–generator power rate is allowed to vary based on the engine–generator power. Empirical knowledge about the operation of a turbo-charged diesel engine suggests that the allowable power rate decreases as the engine power increases. To develop this constraint map, a three-step discrete optimization process is used by sequentially combining genetic algorithm (GA) and exhaustive search (ES). GA results are used to narrow down the design space. Then, ES finds the optimal solution within the search region reduced by GA. A quasi-static map for soot emissions is considered as a first step to evaluate the benefits of including the power rate constraint map in an MPC-based power management for soot emission
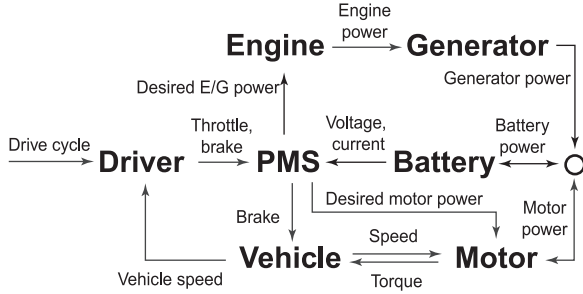
Fig. 1. Series hybrid configuration considered in this paper.

TABLE I
VEHICLE SPECIFICATION

Parameter	Symbol	Value	Unit
Weight	M_{veh}	15554	kg
Frontal Area	A_{veh}	5.72	m^2
Diesel Engine Power	P_e	261	kW
Generator Power	P_g	236	kW
Battery Capacity	C_b	9.27	kWh
Motor Power	P_m	380	kW

Fig. 2. Quasi-static engine maps. (a) Steady-state fuel rate as a function of engine–generator power. (b) Brake-specific fuel consumption *bsfc* of the engine–generator unit superimposed by optimal operation line.

reduction. This constraint map is then experimentally evaluated using an engine-in-the-loop simulation setup where the engine is a physical component and the remaining components of the vehicle system are mathematically modeled. Moreover, the implementation of the resulting PMS on battery life is assessed using a weighted ampere-hour (Ah) processed model [17].

This paper is organized as follows. Section II addresses the formulation of the MPC-based power management in the SHEV along with the cost function and constraints. This section lays out the framework that is used as a tool to evaluate the main contribution of this paper, i.e., the power rate constraint map. The three-step discrete optimization process to design the power rate constraint map is described in Section III. Experimental setup and results are presented and discussed in Section IV, and conclusions are drawn in Section V.

II. MODEL PREDICTIVE CONTROL BASED POWER MANAGEMENT

The SHEV configuration considered in this paper consists of an engine, a generator, in-hub motors, a battery, a driver, and a vehicle, as shown in Fig. 1. Electrical power flow among the generator, battery, and electric motors is managed by a PMS. This paper considers a hybridized mine-resistant ambush-protected all-terrain vehicle whose specifications are summarized in Table I. Quasi-static maps and dynamic equations used to model the SHEV are given in Appendix A.

For power management in the SHEV, MPC is used to split the power demand between the engine–generator unit and the battery. MPC is an attractive control method with advantages such as generating a suboptimal solution in a causal manner and taking into account input and state constraints over a finite horizon. In MPC, an optimal control sequence is computed at each time step by solving an online optimization problem over a finite future time horizon by utilizing a receding horizon approach. Then, the first element of the optimal sequence is applied to the system as a control input, and this procedure is repeated at each time step.
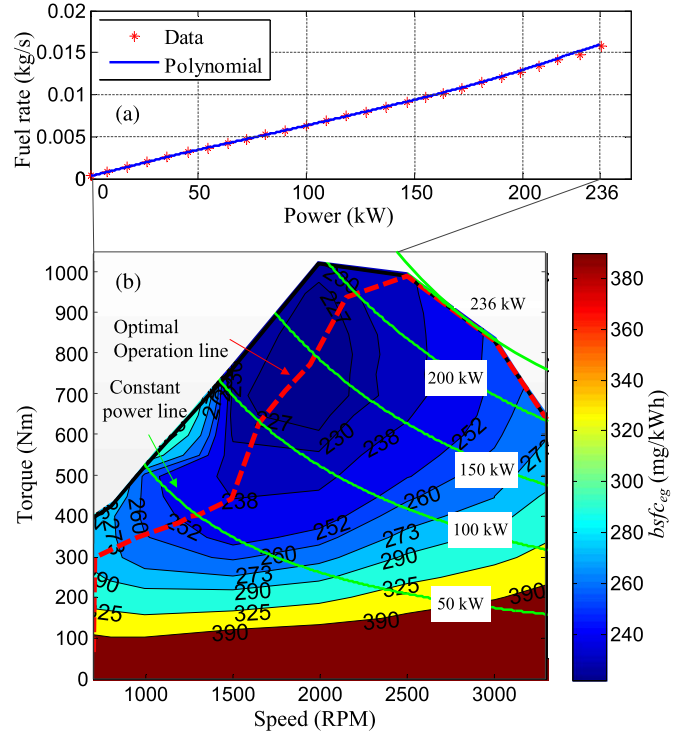
A. Control-Oriented Model

For the purpose of designing a supervisory controller, a simplified modeling approach is considered for the powertrain. To model the battery, a reduced-order equivalent circuit model with a single state is considered. As discussed in [18] and [16], the single-state equivalent circuit model is capable of capturing the SOC dynamics of the battery, the most relevant dynamics, for the supervisory control design. Specifically, the SOC dynamic behavior of the battery is simplified by the following equation:

$$\frac{dx(t)}{dt} = -\frac{V_{\text{oc}} - \sqrt{V_{\text{oc}}^2 - 4R_s u(t)}}{2R_s C_b} \qquad (1)$$

where x is the state of the battery system SOC, and u is the battery power P_b. The battery capacity is denoted by C_b. Open-circuit voltage (OCV) V_{oc} and internal resistance R_s are taken from [19] and tabulated in lookup tables. In general, V_{oc} and R_s are functions of operating temperature and SOC; however, in this paper, they are implemented as functions of SOC only under the assumption of perfect battery cooling.

In the engine–generator in the full SHEV model, a first-order low-pass filter is used to emulate the transient response of a turbocharger. No significant effect of this time lag is observed in the engine–generator operation with the maximum power rate adopted from [20]. Thus, the dynamics of the fuel controller and associated turbo lag are not included in the supervisory controller. Quasi-static maps representing the relationship between power and fuel rate, as well as corresponding speed and torque, are shown in Fig. 2.

Engine–generator power $v(= P_g)$ is calculated by

$$v(t) = P_d(t) - u(t) \tag{2}$$

explaining how the power demand generated by the driver P_d is satisfied by the sum of the battery power u and engine–generator generator power v. In the interest of structuring the MPC problem with a quadratic cost function, the outputs are chosen as follows:

$$y = \begin{bmatrix} x & \dot{m}_f^{0.5} \end{bmatrix}^T \tag{3}$$

where $\dot{m}_f$ is the fuel rate of the engine–generator. Note that the choice of $\dot{m}_f^{0.5}$ is deliberate; the objective is to penalize fuel consumption over the prediction horizon.

In summary, the nonlinear powertrain model is described in the state space representation as follows:

$$\dot{x} = f(x, u)$$
$$y = g(x, v) \tag{4}$$

where $x \in \mathbb{R}^1$, $u \in \mathbb{R}^1$, $v \in \mathbb{R}^1$, and $y \in \mathbb{R}^2$.

B. MPC Formulation

A linear discrete-time MPC control strategy is used for power management. Since the system is nonlinear, linearization and discretization processes are required to formulate a linear MPC problem. A linear discrete-time model can be obtained as

$$x(k+1) = A_d x(k) + B_d u(k) + S_d,$$
$$y(k) = C x(k) + H v(k) + G \tag{5}$$

where $A_d \approx 1 + A\Delta t$, $B_d = B\Delta t$, $S_d = S\Delta t$, and Δt is the sampling period. System matrices are calculated by

$$A = \left.\frac{\partial f}{\partial x}\right|_{(x_0, u_0)} \quad B = \left.\frac{\partial f}{\partial u}\right|_{(x_0, u_0)}$$
$$C = \left.\frac{\partial g}{\partial x}\right|_{(x_0, v_0)} \quad H = \left.\frac{\partial g}{\partial v}\right|_{(x_0, v_0)}$$
$$S = f(x_0, u_0) - (A x_0 + B u_0)$$
$$G = g(x_0, v_0) - (C x_0 + H v_0) \tag{6}$$

where x_0, u_0, and v_0 are the values at previous sampling time $t - 1$.

For the purpose of MPC, the cost function J_1 to be minimized and constraints are defined as

$$J_1(k) = \sum_{i=k}^{k+N_p} (y(i|k) - y_{\text{ref}})^T \begin{bmatrix} w_1 & 0 \\ 0 & w_2 \end{bmatrix} (y(i|k) - y_{\text{ref}})$$
$$+ \Delta v(i|k)^T w_3 \Delta v(i|k) + u(i|k)^T w_4 u(i|k)$$

$$\text{s.t.} \quad P_{b,\min} \le u(i|k) \le P_{b,\max}, \; i = 1, 2, \dots, N_c$$
$$P_{g,\min} \le v(i|k) \le P_{g,\max}, \quad , i = 1, 2, \dots, N_c$$
$$\Delta P_{g,\min} \le \Delta v(i|k) \le \Delta P_{g,\max}, \; i = 1, 2, \dots, N_c$$
$$\text{SOC}_{\min} \le y_1(i|k) \le \text{SOC}_{\max}, \; i = 1, 2, \dots, N_p \tag{7}$$

where N_p and N_c are lengths of the prediction and control horizons, respectively. Parameter $w_j \ (j = 1, \dots, 4)$ represents a weighting factor for the balance between battery SOC regulation and fuel economy improvement. These weighting factors are tuned through repeated simulations until the fuel economy improvements are diminished. Variables $P_{g,\min}$ and $P_{g,\max}$ are the minimum and maximum engine–generator power values, respectively. The minimum and maximum power rates of the engine–generator, i.e., $\Delta P_{g,\min}$ and $\Delta P_{g,\max}$, are constants adopted from [20] enabling the implicit control of soot emissions. Maximum discharging and charging power limits of the battery can be obtained by the following equations:

$$P_{b,\max} = V_{\min} \frac{(V_{oc} - V_{\min})}{R_s} \tag{8}$$

$$P_{b,\min} = V_{\max} \frac{(V_{\max} - V_{oc})}{R_s} \tag{9}$$

where $V_{\max}$ and $V_{\min}$ represent manufacturer-specified maximum and minimum voltage limits, respectively.

Equation (7) is rewritten as a quadratic programming (QP) problem

$$\min_{\Delta U} \quad J_1 = \frac{1}{2}\Delta U^T \boldsymbol{\Psi_1} \Delta U + \boldsymbol{\Psi_2^T} \Delta U$$
$$\text{s.t.} \quad \boldsymbol{\Gamma_1} \Delta U \le \boldsymbol{\Gamma_2} \tag{10}$$

where $\Delta U = [\Delta u(k|k), \dots, \Delta u(k + N_c - 1|k)]^T$ is the change in the input vector. The lengths of horizon for control and prediction, i.e., N_c and N_p, respectively, are tuned based on the computation time so that the time of solving the optimization problem is less than the time step of 0.2 s to allow real-time simulations with the hardware in the loop. Matrices $\boldsymbol{\Psi_1}$, $\boldsymbol{\Psi_2}$, $\boldsymbol{\Gamma_1}$, and $\boldsymbol{\Gamma_2}$ are obtained by substituting (2) and (5) into (7) (see Appendix B).

Power demand over the prediction horizon is assumed constant

$$P_d(k + i|k) = P_d(k|k), \quad i = 1, \dots, N_p. \tag{11}$$

Although this assumption may not be accurate, unsteady power demands can be properly handled due to the fact that only the first element of the control action sequence over the prediction horizon is used. Approaches to predict future power demand such as an exponential decay, stochastic and perfect predictions, and their influence on the fuel economy are not considered in this paper but can be found in [21] and [22].

After solving the QP problem (10), the first element of optimal sequence $\Delta u_{\text{opt}}(k|k)$ is used to split power demand, i.e., optimal engine–generator power v_{opt} is calculated by

$$v_{\text{opt}}(k) = P_d(k) - u(k - 1) - \Delta u_{\text{opt}}(k|k). \tag{12}$$

C. Verification and Generation of the Benchmark Results

The purpose of this section is to verify the implementation of the MPC problem described so far and to generate a benchmark for the simulation-based optimal design of the power rate constraint map.
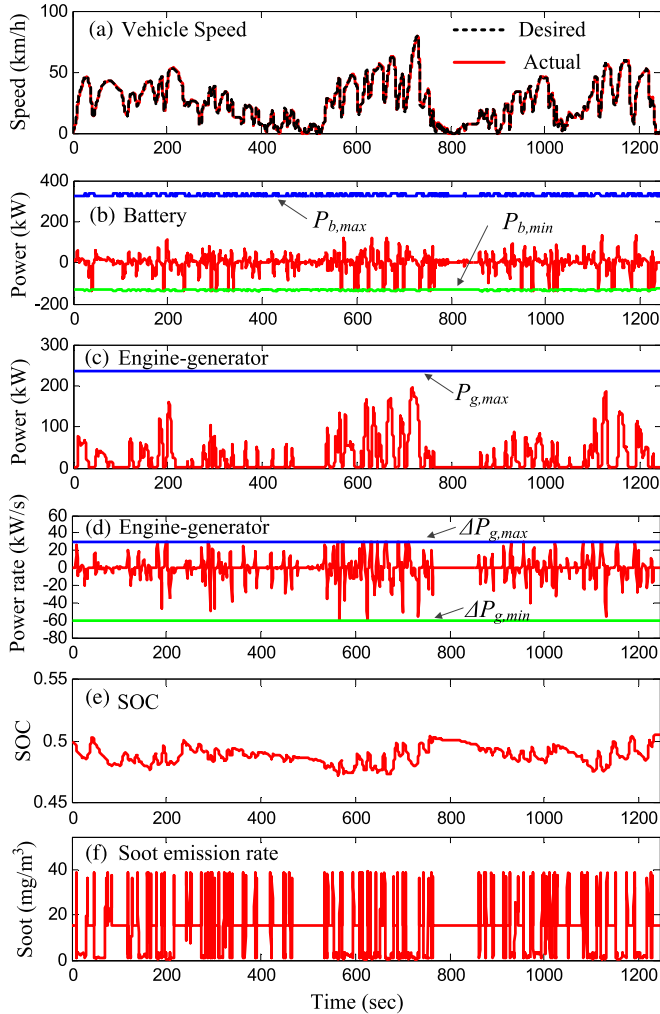
Fig. 3. Simulated transient behaviors under MPC-based PMS over UAC. (a) Vehicle speed, (b) battery power, (c) battery SOC, (d) engine–generator power, (e) engine–generator power rate, and (f) soot emission rate.

TABLE II
PARAMETER AND CONSTRAINT VALUES FOR MPC

MPC Parameter	Value	Constraint	Value
w_1	4.17	$V_{\min}$	2.0 V
w_2	1	$V_{\max}$	3.6 V
w_3	2.5e-5	$P_{g,\min}$	0 kW
w_4	1.25e-6	$P_{g,\max}$	236 kW
N_c	15	$\Delta P_{g,\min}$	-60 kW/s
N_p	40	$\Delta P_{g,\max}$	30 kW/s
$y_{1,\text{ref}}$	0.5	$SOC_{\min}$	0.3
$y_{2,\text{ref}}$	0	$SOC_{\max}$	0.7

MPC problem are summarized in Table II, along with the constraint values.

To predict the trends in soot emissions and subsequently help with the control design, a quasi-static map is considered. Note that more than 50% of all soot emissions could be generated during transients such as tip-in operations [20], and hence, a quasi-static map cannot accurately predict the magnitude of the soot emissions during aggressive transients. Nevertheless, for the purpose of designing a supervisory controller, quasi-static maps have been shown to be useful for their ability to capture the basic trends [24], [25]. More relevantly, the quasi-static soot emissions map used in this paper has been previously found adequate to capture the basic trends in soot emissions even during transients [26]. Therefore, it is used in this paper to help with the control design and avoid ad hoc experimental tuning, with the understanding that the resulting control design may not yield the optimal performance and a dynamic soot emissions model such as [26] would ultimately be required to achieve the best performance.

Simulation results with the MPC-based PMS are given in Fig. 3. Fig. 3(a) shows that the vehicle can follow the desired speed profile, which means that the power demands from the driver are satisfied by the engine–generator unit and the battery under the MPC-based power management. As shown in Fig. 3(b)–(d), powertrain components such as the battery and the engine–generator unit operate without exceeding the minimum and maximum bounds of desirable range. The battery SOC is well regulated around the target value of 0.5 between 0.3 and 0.7, as shown in Fig. 3(e). Fig. 3(f) shows the resulting simulated soot emissions rate of the diesel engine. Fuel economy and total soot emission predicted over the UAC are 3.278 km/l (7.71 mi/gal) and 0.0316 g/km, respectively, which are used as the baseline values for the simulation-based results.

D. Effect of Maximum Engine–Generator Power Rate

To investigate the effect of the engine–generator power rate on the fuel economy and soot emissions, different maximum power rates are simulated. The minimum power rate is considered to be a fixed parameter for two reasons: 1) Soot emissions are zero during braking because of fuel cutoff; 2) the slow decrease in power leads to multiple power conversions, resulting in a decrease in the total efficiency of the system, as explained in [15].

As shown in Fig. 4, a decrease in the maximum power rate of the engine–generator helps reduce the soot emissions, but it decreases fuel economy as a tradeoff. Specifically, considering

The SHEV is simulated in a forward-looking scheme, where the driver determines control commands to follow a desired speed profile. A military vehicle driving cycle, i.e., an urban assault cycle (UAC) shown in Fig. 3(a), is used to investigate the performance of the MPC-based PMS. This cycle with a total distance of 8.80 km (5.46 mi) is aggressive compared with a federal driving cycle such as the Urban Dynamometer Driving Schedule for Heavy-Duty Vehicles. The UAC has frequent high-acceleration and high-deceleration events, typical of military driving conditions [23].

For the purpose of accounting for the remaining battery SOC, two consecutive driving cycles are considered, and the fuel economy is calculated by

$$\text{fuel economy} = \frac{1}{N_s} \sum_{k=1}^{N_s} \frac{\int_{t_k}^{t_k+t_{\text{cycle}}} v_{\text{veh}} dt}{\int_{t_k}^{t_k+t_{\text{cycle}}} \dot{m}_f dt} \quad (13)$$

where t_{cycle} is the total time of the given driving cycle, v_{veh} is the velocity of the vehicle, and N_s is the total number of t_k's that satisfies the SOC sustainability condition $t_k \in \{\xi : SOC(\xi) = SOC(\xi + t_{\text{cycle}})\}$ and $\xi \in \mathbb{R}^1$. Parameters for the
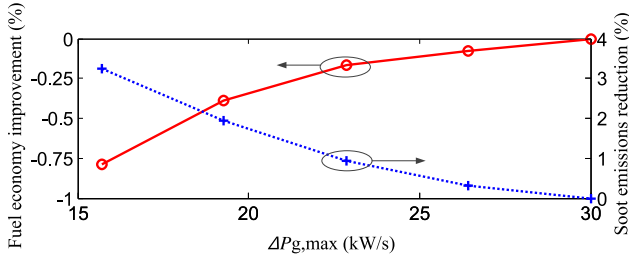
Fig. 4.   Effect of a decrease in the maximum engine–generator power rate on fuel economy and soot emissions.

a reduction of less than 0.5% in fuel economy as a reasonable compromise, limiting the maximum power rate to 19.3 kW/s could reduce soot emissions by 1.9%.

This example is useful to demonstrate the tradeoff between soot emissions and fuel economy; however, it also raises the question of whether a constant maximum power rate is the best way to address this tradeoff. This question is addressed in the next section. Specifically, it is shown that better smoke results can be obtained if the maximum power rate is not constant but variable, i.e., the rate depends on the engine–generator power level.

III. MAXIMUM POWER RATE MAP DESIGN

This section describes the offline process of optimizing the maximum power rate $\Delta P_{g,\max}$ as a function of the engine–generator power to minimize the total soot emission over a driving cycle.

The discrete optimization problem is formulated by

$$\min_{\Delta P_{g,\max}(d)} \quad J_2 = \frac{1}{N_s} \sum_{k=1}^{N_s} \int_{t_k}^{t_k+t_{\text{cycle}}} \dot{m}_{\text{soot}} dt$$

$$\text{s.t.} \quad \alpha \geq \underline{\alpha}$$

$$d = h(P_g) \in \{d_1, d_2, \ldots, d_{l_1}\}$$

$$d_i \subset \mathbb{R}_{\geq 0}, \ i = 1, 2, \ldots, l_1$$

$$\Delta P_{g,\max}(d) \in \{\beta_1, \beta_2, \ldots, \beta_{l_2}\}$$

$$\beta_j \in \mathbb{R}_{>0}, \ j = 1, 2, \ldots, l_2 \quad (14)$$

where $\dot{m}_{\text{soot}}$ is the soot emissions rate, and α is the fuel economy defined in (13). The minimum allowed fuel economy $\underline{\alpha}$ is set to 3.265 km/l (7.68 mi/gal), i.e., fuel economy is allowed to be reduced from 3.278 km/l (7.71 mi/gal) to 3.265 km/l (7.68 mi/gal) by 0.4%. The reference fuel economy is obtained from the MPC-based power management without the optimized power rate constraint map. Function h is a discrete mapping from the engine–generator power P_g to partitions of power capability of the engine–generator d_i, e.g., $d_1 = [0 \ 25)$ kW and $d_2 = [25 \ 50)$ kW. In each partition d_i, the maximum power rate $\Delta P_{g,\max}$ is set to β_j, and lower and upper bounds of β_j are defined by considering vehicle requirements and engine soot generation. Integer variables l_1 and l_2 denote the number of design variables (i.e., the power rates for different d_i's) and
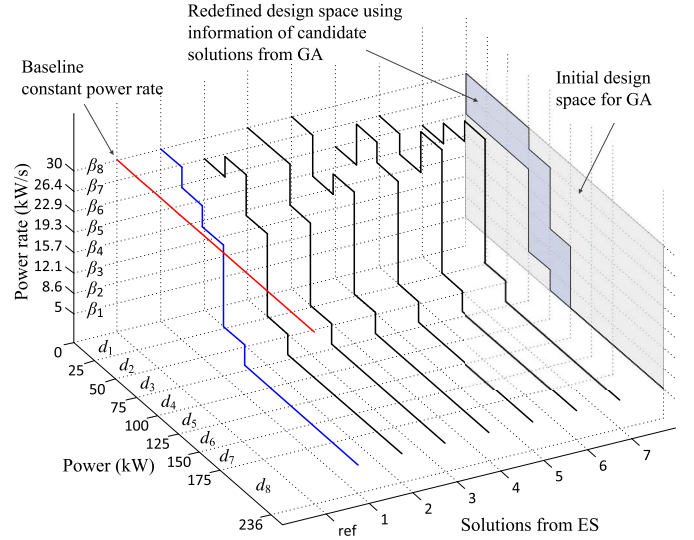

Fig. 5.   Optimal solutions from ES to adjust the maximum power rate of the engine–generator depending on power level.

TABLE III
INPUT PARAMETERS OF GA

Parameter	Value
Number of population	30
Number of generation	50
Probability of crossover	0.8
Probability of mutation	0.01

the size of design space (i.e., the discrete set of values that the power rates can assume), respectively.

With respect to solving this discrete optimization problem, algorithms such as GA and simulated annealing are good for searching the global optimum; thus, those algorithms have been applied to optimize the design and control strategy of HEVs [27]–[30]. However, a large number of iterations are required to guarantee global optimality, which is a challenge in our study, since each iteration takes several minutes in vehicle simulation. To overcome this drawback, a three-step discrete optimization process is conducted.

1) Find candidate solutions using GA.
2) Redefine the lower and upper bounds for each variable.
3) Determine the optimal solution using ES in the bounded range.

Fig. 5 and Table III provide the parameters for the optimization problem (14) and the parameters for GA, respectively. It is noted that the total number of every possible case in the initial design space (see the gray shaded area in Fig. 5) is 8^8, which is impractical to apply ES. However, the search region is significantly reduced by using GA results, as shown in the blue-shaded area in Fig. 5. Thus, only 648 cases, i.e., 0.004% of every possible case, need to be explored by ES. Then, the optimal power rate constraint map, which is the blue line in Fig. 5, is obtained from ES results and compared with seven power rate constraint maps, resulting in the fewest soot emissions over the UAC. All of the power rate constraint maps enforce the power rate of the engine–generator to be decreased with power above 75 kW. This result means that these solutions behave effectively as a low-pass filter, incorporating load leveling, as used in [15].
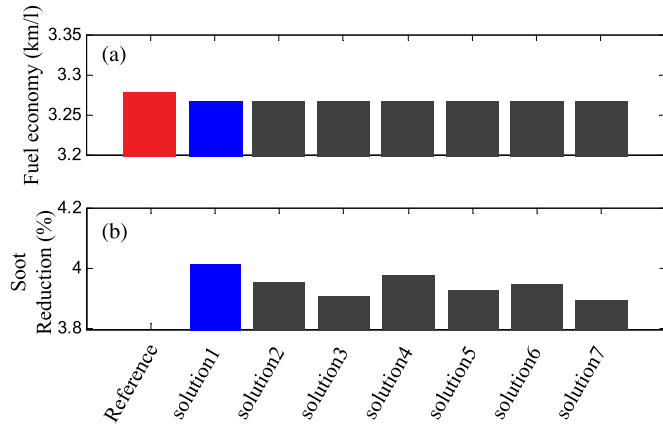
Fig. 6. Simulation-based comparison of solutions from ES with reference. (a) Fuel economy and (b) reduction in soot emissions.

Fig. 6 summarizes the reduction in soot emissions and the compromise in fuel economy from the model-based simulation. The total soot emission could be successfully reduced by 4.0% with the optimal power rate constraint map without a significant compromise in fuel economy; fuel economy is reduced by only 0.4%. This is two times the reduction in soot emissions obtained with a constant maximum engine power rate constraint in Section II-D.

The results reported thus far are simulation based and are obtained using a quasi-static map for soot emissions. While the quasi-static map is useful for our design purposes, it is reasonable to expect the actual reduction in soot emissions to be higher than what is predicted by the quasi-static map. Therefore, to better assess the extent to which the power rate constraint map can reduce soot emissions, this map is experimentally evaluated in an engine-in-the-loop simulation framework, as described in the following section.

IV. EXPERIMENTAL RESULTS

For experimental evaluation, a networked engine-in-the-loop simulation [31]–[33] of the vehicle system is considered, where the engine is the hardware component and the remaining components of the vehicle system (i.e., generator, battery, motors, vehicle dynamics, and driver) are mathematically modeled, as described in Appendix A. The overview of the networked system architecture is shown in Fig. 7.

A. Engine-in-the-Loop Setup

The hardware component of interest for this paper is a Navistar 6.4-L V8 diesel engine with 260-kW rated power at 3000 r/min and a rated torque value of 880 Nm at 2000 r/min. It is intended for a variety of medium-duty truck applications covering the range between classes IIB and VII and features technologies such as high-pressure common rail fuel injection, twin sequential turbochargers, and exhaust gas recirculation. A high-fidelity ac electric dynamometer couples the physical engine with the simulation models in real time and operates in speed control mode. The setup can be connected to Simulink for integration with mathematical models, allowing for a real-time
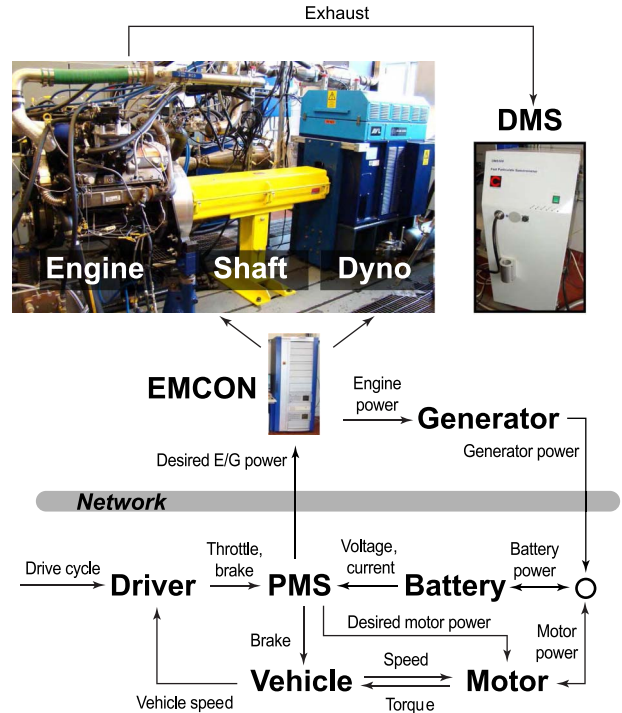

Fig. 7. Overview of the engine-in-the-loop vehicle system simulation architecture used in this case study. The engine model used for MPC development is replaced with an actual engine.

hardware-in-the-loop simulation. This connection is achieved through an EMCON 400 flexible test bed with an ISAC 400 extension.

Transient soot emissions are measured with a differential mobility spectrometer (DMS) 500 manufactured by Cambustion Ltd. in the form of temporally resolved particulate concentrations. DMS 500 offers measurement of different particle sizes by identifying the mobility of particles with a sampling frequency of 10 Hz and a response time of 200 ms. Therefore, DMS 500 makes it possible to analyze the time evolution of the soot emissions.

B. Experimental Results and Discussion

The MPC-based PMS with the power rate constraint map is implemented in the SHEV model and evaluated via the engine-in-the-loop test setup. The constraint map obtained from the simulation-based design is directly utilized in the experiments without any further tuning. Since the electrometer detectors are sensitive and show drift when the detectors are exposed to high concentrations for a long time (e.g., 4 min), only the middle part of the UAC, i.e., the most aggressive part, is used for the measurement of soot emissions. Fuel consumption is measured over the entire UAC.

To highlight the performance of the strategy, specific time periods from 100 to 200 s are shown in Fig. 8. As shown in Fig. 8(a), there is no difference in vehicle speed with and without the power rate constraint map, implying that the vehicle performance in this drive cycle is not deteriorating when the map is introduced. The responses of the battery and the engine–generator are influenced by the power rate constraint
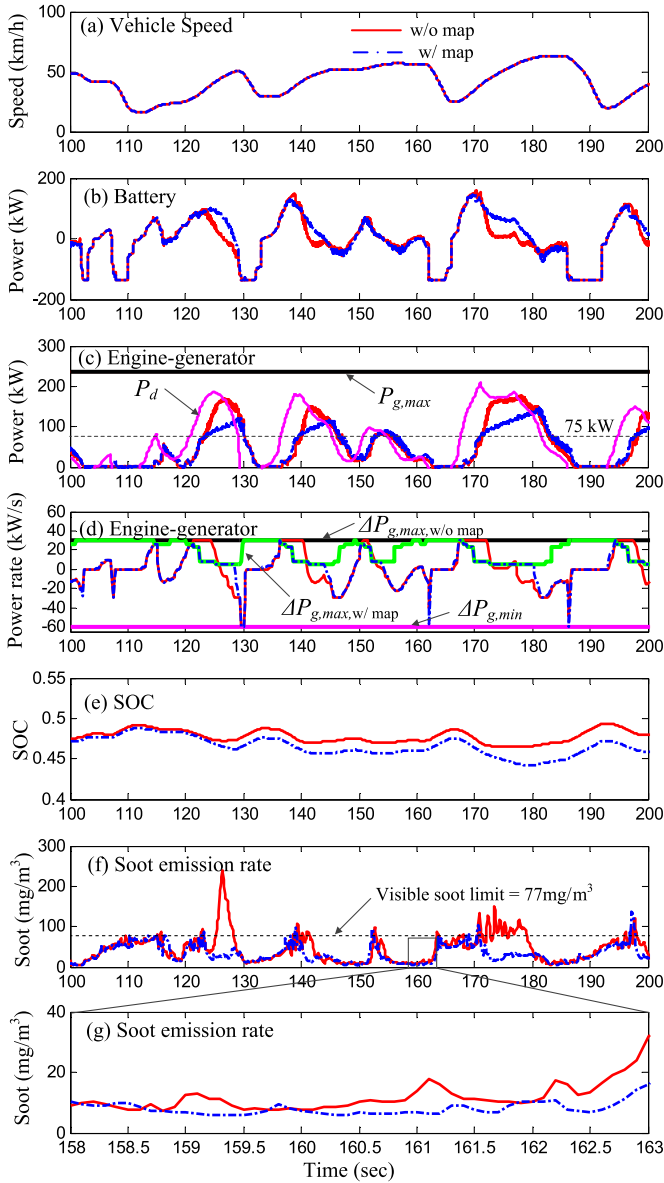
Fig. 8. Transient behaviors with and without the power rate constraint map over UAC. (a) Vehicle speed, (b) battery power, (c) engine–generator power, (d) engine–generator power rate, (e) battery SOC, (f) soot emission rate, and (g) soot emissions rate (158–163 s).
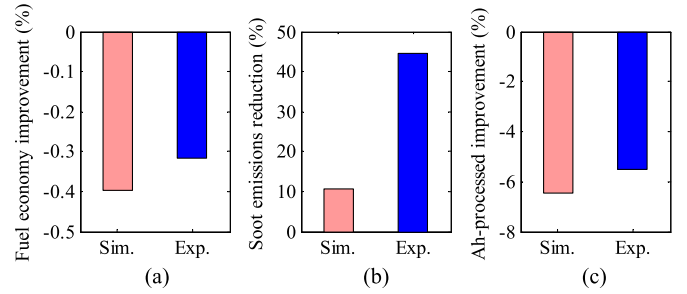

Fig. 9. Comparison of percentage improvement in performance from the simulations and experiments using the power rate constraint map: (a) fuel economy, (b) soot emissions, and (c) effective Ah processed; soot emissions in the experiments are measured for 240 s in the middle part of the military cycle since the electrometer detectors show drift when they are exposed to high concentrations for a long time period.
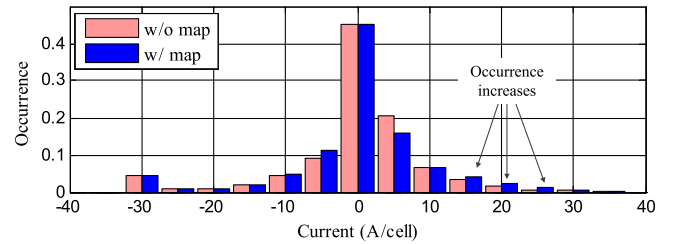

Fig. 10. Histogram of current of the battery cell. Using the power rate constraint map leads to an increase in the occurrence of current rates between 15 and 25 A/cell as a tradeoff.

map, as shown in Fig. 8(b) and (c). Above the power level of 75 kW, the map enforces the engine–generator to provide power gradually, i.e., over 75 kW, the maximum power rate becomes an active constraint, as shown in Fig. 8(d). Fig. 8(f) shows that soot emissions are dramatically reduced whenever the power rate is limited: 75% of peak value of soot emissions can be reduced by smooth engine–generator operations. When the engine–generator power rate is limited, soot emissions are implicitly controlled to within an upper bound, which is around 77 mg/m^3, i.e., the minimum concentration at which soot emissions are visible [7].

The benefit of using the power rate constraint map is observed not only during aggressive increase in power demand but also during the near-idle regions following the peak demands. In the high-power-demand regions, since the engine–generator power is slowly increased, the remainder of the power demand

needs to be satisfied by the battery, resulting in lower battery SOCs, as shown in Fig. 8(b) and (e). Consequently, the engine–generator has to charge the battery for SOC regulation when vehicle power demand is not high, avoiding high soot emissions near the engine-idling condition, as shown in Fig. 8(g).

As a result of using the power rate constraint map, the total soot emission is reduced by 44.5% without significantly compromising fuel economy: Fuel economy is reduced from 3.150 km/l (7.41 mi/gal) to 3.142 km/l (7.39 mi/gal) by only 0.3%. Results for the fuel economy and total soot emission obtained in simulations and experiments are compared and summarized in Fig. 9(a) and (b). As expected, the soot emission reduction performance observed in the experiments exceeds the prediction of the simulations because the quasi-static soot emissions map used in the simulations does not fully capture the magnitude of soot emissions during transients. These results could lead to additional benefits that are beyond the scope of this paper. For example, a reduction in engine-out soot emissions could positively affect the design and control of the diesel particulate filter in the aftertreatment system.

This significant reduction in soot emissions with only a minor compromise in fuel economy is not achieved without a cost. Fig. 10 highlights the cost in terms of the battery usage. Since the battery provides propulsion power when the engine power is actively limited by the power rate constraint map, the occurrence of current rates between 15 and 25 A/cell increases, which could translate to an increase in battery degradation as a tradeoff.

To estimate the additional battery degradation over the driving cycle due to the power rate constraint map, the effective Ah-processed model in [17] is used. This approach is based on the fatigue analysis under the assumption of linear cumulative damage. The effective accumulated Ah processed is calculated by

$$Ah_{eff} = \int_0^{t_f} \kappa(T_b, SOC)|I|dt \tag{15}$$

where the severity factor κ is a nonlinear function of operating temperature T_b and SOC. The severity factor collapses in our case to a constant because of the narrow operating range of the battery SOC and assumed perfect battery cooling. As shown in Fig. 9(c), the effective accumulated Ah processed increases from 3.51 to 3.71 Ah by 5.5% due to the power rate constraint map. This increase in Ah processed could lead to a corresponding decrease in battery life.

V. CONCLUSION

An MPC-based PMS has been developed to reduce soot emissions in a diesel SHEV with a minimal compromise in fuel economy. This objective is achieved through a constraint map to adjust the maximum allowable power rate of the engine–generator unit. A QP is used to solve the MPC problem to split power demand between the engine–generator unit and the battery. To obtain the power rate constraint map for minimal soot emissions, a three-step discrete optimization process has been conducted by sequentially utilizing GA and ES.

The engine performance with respect to soot emissions and fuel economy using the power rate constraint map has been experimentally evaluated. Experimental results show that the regulated engine operation using the proposed power rate constraint map results in reduced soot emissions. Quantitatively, the total soot emission is reduced by 44.5%, whereas fuel economy is compromised by only 0.3%. Battery statistics show that the PMS with the constraint map increases the medium-level current operations as a tradeoff. Specifically, the Ah processed increases by 5.5%, and a corresponding decrease could be expected in the battery capacity.

As a first step to consider fuel economy and soot emissions simultaneously in an MPC-based supervisory control framework, this paper utilized a quasi-static soot emissions map. A transient soot emissions model could improve the performance even further. Therefore, developing such a model and evaluating its performance within the methodology presented in this paper is an important direction for future research. In addition, the influence of the power demand prediction on the performance will be investigated.

APPENDIX A

This Appendix presents the SHEV system model.

Figs. 11 and 12 show the engine torque and soot emission maps obtained from a Navistar 6.4-L V8 diesel engine in [26]. The engine torque map is augmented by a PI fuel controller
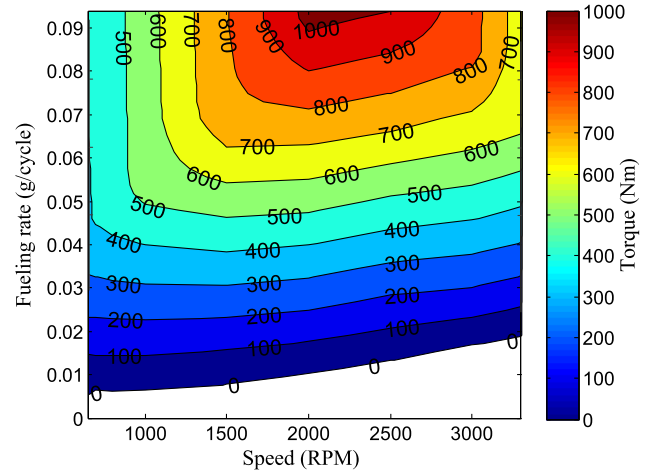

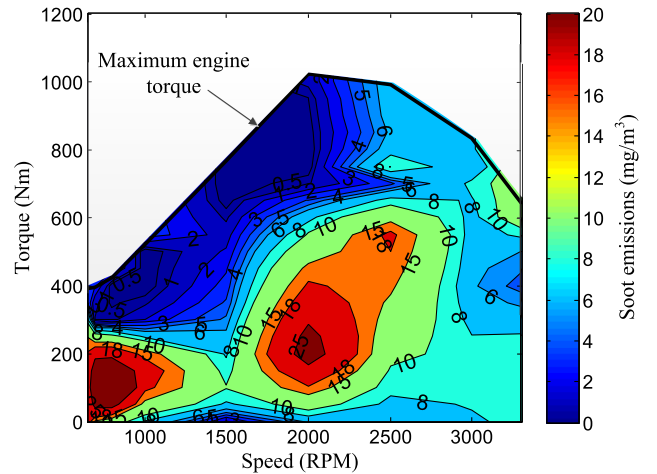Fig. 11. Engine torque map as a function of speed and fuel rate.

Fig. 12. Soot emissions map as a function of speed and torque.

submodel generating the engine rack position ($\zeta(t) \in [0,1]$), which is given by

$$\zeta(t) = k_P \Delta\tau_e + k_I \int \Delta\tau_e dt$$

where $\Delta\tau_e$ is the error between the desired and actual engine torque values; and k_P and k_I are proportional and integral gains, respectively. This PI controller is implemented only to allow for a stable virtual coupling between the physical engine and the generator model. In a real application, or in an experimental setup with a physical engine and physical generator mechanically coupled, this PI controller and the engine torque measurement would not be necessary. Instead, the engine/generator speed would be measured and regulated.

To represent the effect of turbocharger lag on transient response during rapid increases of engine rack positions, the fuel mass is filtered by a first-order filter. The engine–generator unit is assumed to be fully warmed up so that the effects of temperature are ignored. Fig. 13 illustrates the efficiency of the generator in [34].

A 9.27-kWh Li-ion battery pack with lithium–iron–phosphate (LiFePO$_4$ or LFP) cells by A123 is considered, and the battery is modeled using an OCV-R-RC-RC equivalent
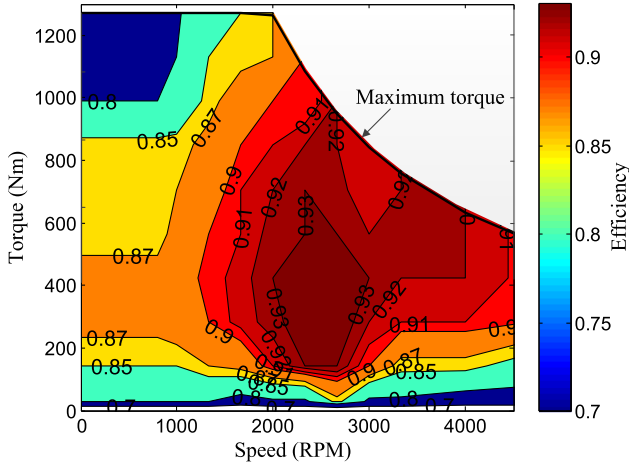
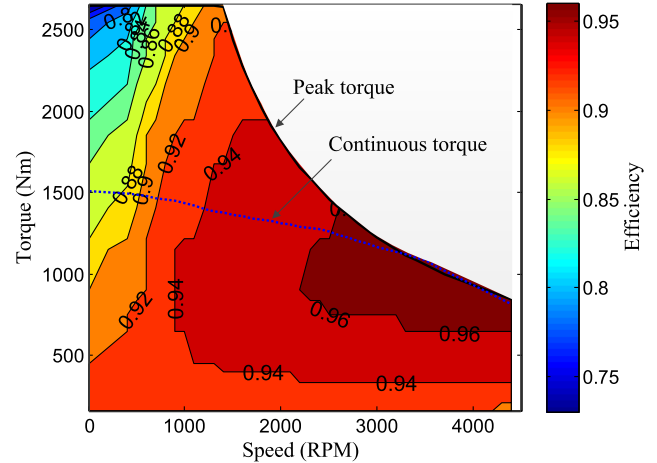Fig. 13. Generator efficiency map as a function of speed and torque.

Fig. 14. Motor efficiency map superimposed by peak and continuous torque values.

TABLE IV
SPECIFICATION OF THE BATTERY

Parameter	Value	Unit
Nominal Voltage	3.3	V
Minimum Voltage	2.0	V
Maximum Voltage	3.6	V
Nominal Capacity	2.3	Ah
Number of Cells in Series	130	-
Number of Cells in Parallel	10	-

circuit approach. The OCV V_{oc}, internal resistances (i.e., R_s, R_1, and R_2), and capacitance values (i.e., C_1 and C_2) during discharging and charging are determined using the parameter identification technique presented in [19]. The specifications for the LFP battery are summarized in Table IV.

The terminal voltage V_t of the battery is calculated by using

$$V_t = V_{oc} - V_1 - V_2 - IR_s$$

where V_1 and V_2 are voltages across C_1 and C_2, respectively, and calculated based on the following dynamic equations:

$$\frac{dV_i}{dt} = \frac{1}{C_i}\left(I - \frac{V_i}{R_i}\right), \quad i = 1, 2.$$

The sign convention is such that positive current denotes battery discharging.

Fig. 14 shows that the efficiency of the motor η_m is expressed as a function of motor torque τ_m and motor speed ω_m. The maximum output torque of the motor $\tau_{m,\max}$ is governed between the continuous torque $\tau_{m,\text{cont}}$ and the peak torque $\tau_{m,\text{peak}}$ accounting for the heat index γ as follows:

$$\tau_{m,\max} = \tau_{m,\text{cont}} + (1 - \gamma)\tau_{m,\text{peak}}$$

$$\frac{d\gamma}{dt} = -\frac{0.3}{180}\left(\frac{\tau_m}{\tau_{m,\text{cont}}} - 1\right), \quad \gamma(0) = 0.3$$

where $\tau_{m,\text{cont}}$ and $\tau_{m,\text{peak}}$ are functions of the motor speed ω_m, as shown in Fig. 14. Heat index γ emulates the change in the torque limit based on operating temperature as introduced in Powertrain Systems Analysis Toolkit (PSAT) developed by the Argonne National Laboratory [34].

A point-mass representation is used for the vehicle. The longitudinal dynamics of the vehicle are calculated through the following equation:

$$M_{\text{veh}}\frac{dv_{\text{veh}}}{dt} = F_{\text{prop}} - F_{\text{brk}} - F_{\text{RR}} - F_{\text{WR}}$$

where M_{veh} is the mass of the vehicle, respectively; F_{prop} is the propulsion force; F_{brk} is the braking force; and F_{RR} is the rolling resistance force expressed by

$$F_{\text{RR}} = f_r M_{\text{veh}} a_g$$

where f_r is the rolling resistance, and a_g is the gravitational acceleration. Wind resistance force F_{WR} is calculated by using

$$F_{\text{WR}} = \frac{1}{2}\rho_{\text{air}}C_d A_{\text{veh}} v_{\text{veh}}^2$$

where ρ_{air} is the air density, C_d is the drag coefficient, and A_{veh} is the frontal area of the vehicle. The road grade is not considered in the driving cycles in this paper.

The driver model, which takes the desired and actual vehicle velocities as inputs and provides propulsion or braking power demands, is adopted from [31] and is a PI controller with saturation and anti-windup.

APPENDIX B

Equation (5) is iterated in order to predict outputs over the future horizon as follows:

$$\begin{bmatrix} \hat{x}(k+1|k) \\ \vdots \\ \hat{x}(k+N_p|k) \end{bmatrix} = \mathbf{A}x(k) + \mathbf{B}\Delta U + \mathbf{B_1} + \mathbf{S}$$

$$\begin{bmatrix} \hat{y}(k|k) \\ \vdots \\ \hat{y}(k+N_p|k) \end{bmatrix} = \mathbf{C}\begin{bmatrix} \hat{x}(k|k) \\ \vdots \\ \hat{x}(k+N_p|k) \end{bmatrix} + \mathbf{H}\begin{bmatrix} \hat{v}(k|k) \\ \vdots \\ \hat{v}(k+N_p|k) \end{bmatrix} + \mathbf{G}$$

where

$$\mathbf{A} = \begin{bmatrix} A_d \\ \vdots \\ A_d^{N_p} \end{bmatrix}, \mathbf{B} = \begin{bmatrix} I & \cdots & 0 \\ \vdots & \ddots & \vdots \\ \sum_{i=0}^{N_p-1} A_d^i & \cdots & \sum_{i=0}^{N_p-N_u} A_d^i \end{bmatrix} B_d$$

$$\mathbf{B_1} = \begin{bmatrix} I \\ \vdots \\ \sum_{i=0}^{N_p-1} A_d^i \end{bmatrix} B_d u(k-1), \mathbf{S} = \begin{bmatrix} I \\ \vdots \\ \sum_{i=0}^{N_p-1} A_d^i \end{bmatrix} S_d$$

$$\mathbf{C} = \mathrm{diag}\underbrace{\begin{bmatrix} C & \cdots & C \end{bmatrix}}_{(N_p+1)\times\dim C}, \quad \mathbf{H} = \mathrm{diag}\underbrace{\begin{bmatrix} H & \cdots & H \end{bmatrix}}_{(N_p+1)\times\dim H}$$

$$\mathbf{G} = \underbrace{\begin{bmatrix} G^T & \cdots & G^T \end{bmatrix}^T}_{(N_p+1)\times\dim G^T}.$$

The sequences of the engine–generator are given by

$$\begin{bmatrix} \hat{v}(k|k) \\ \vdots \\ \hat{v}(k+N_p|k) \end{bmatrix} = \mathbf{P_d} - \mathbf{u_0} - \mathbf{K_1}\Delta U$$

with

$$\mathbf{P_d} = \begin{bmatrix} P_d(k|k) & \cdots & P_d(k+N_p|k) \end{bmatrix}^T$$

$$\mathbf{u_0} = \underbrace{\begin{bmatrix} u(k-1) & \cdots & u(k-1) \end{bmatrix}^T}_{(N_p+1)\times 1}$$

$$\mathbf{K_1} = \begin{bmatrix} 1 & 0 & \cdots & 0 \\ \vdots & \ddots & \vdots & \vdots \\ 1 & 1 & 1 & 1 \\ \vdots & \vdots & \vdots & \vdots \\ 1 & \cdots & \cdots & 1 \end{bmatrix}_{(N_p+1)\times N_c}.$$

The outputs over the prediction horizon can be expressed by

$$\mathbf{Y} = \mathbf{C_1} x(k) + \mathbf{\Phi_1}\Delta U + \mathbf{\Phi_2}$$

where

$$\mathbf{C_1} = \mathbf{C}\begin{bmatrix} I \\ \mathbf{A} \end{bmatrix}, \quad \mathbf{\Phi_1} = \mathbf{C}\begin{bmatrix} 0 \\ \mathbf{B} \end{bmatrix} - \mathbf{K_1}, \quad \mathbf{\Phi_2} = \begin{bmatrix} 0 \\ \mathbf{B_1} \end{bmatrix} + \mathbf{H} + \begin{bmatrix} 0 \\ \mathbf{S} \end{bmatrix} + \mathbf{G}.$$

Finally, matrices for the QP (7) can be computed as follows:

$$\mathbf{\Psi_1} = 2\left(\mathbf{\Phi_1}^T W_1 \mathbf{\Phi_1} + \mathbf{K_1}^T W_2 \mathbf{K_1} + W_3\right)$$

$$\mathbf{\Psi_2} = 2\left(x(k)^T \mathbf{C_1}^T + \mathbf{\Phi_2}\right) W_1 \mathbf{\Phi_1}$$
$$\quad - 2\left((\mathbf{K_1}^T\mathbf{K_1})^{-1}\mathbf{K_1}(\mathbf{P_d} - \mathbf{u_0} - \mathbf{v_0})\right)^T W_2 + 2\mathbf{u_0} W_3 \mathbf{K_1}$$

$$\mathbf{\Gamma_1} = \begin{bmatrix} \mathbf{K_2} \\ -\mathbf{K_2} \\ \mathbf{K_2} \\ -\mathbf{K_2} \\ I \\ -I \\ -\mathbf{B} \\ \mathbf{B} \end{bmatrix}, \quad \mathbf{\Gamma_2} = \begin{bmatrix} \mathbf{P_{b,max}} - \mathbf{u_0} \\ -\mathbf{P_{b,max}} + \mathbf{u_0} \\ \mathbf{P_d} - \mathbf{u_0} \\ \mathbf{P_{g,max}} - \mathbf{P_d} + \mathbf{u_0} \\ \mathbf{K_2}^{-1}(\mathbf{u_0} + \mathbf{v_0} - \mathbf{P_d}) + \Delta\mathbf{P_{g,max}} \\ \mathbf{K_2}^{-1}(\mathbf{P_d} - \mathbf{u_0} - \mathbf{v_0}) - \Delta\mathbf{P_{g,min}} \\ \mathbf{A}x(k) + \mathbf{B_1} + \mathbf{S} - \mathbf{SOC}_{min} \\ -\mathbf{A}x(k) - \mathbf{B_1} - \mathbf{S} + \mathbf{SOC}_{max} \end{bmatrix}$$

where

$$\mathbf{K_2} = \begin{bmatrix} 1 & 0 & \cdots & 0 \\ \vdots & \ddots & \vdots & \vdots \\ 1 & 1 & 1 & 1 \end{bmatrix}_{N_c \times N_c}.$$

REFERENCES

[1] T. W. Asmus, "A manufacturer's perspective on IC engine technology at century's end," in *Proc. Fall Tech. Conf. ASME Intern. Combust. Engine Div.*, 1999, vol. 1, pp. 1–10.

[2] F. Tavares, R. Johri, A. Salvi, S. Baseley, and Z. S. Filipi, "Hydraulic hybrid powertrain-in-the-loop integration for analyzing real-world fuel economy and emissions improvements," presented at the Soc. Automotive Eng. Commercial Vehicle Eng. Congr., Rosemont, IL, USA, 2011, SAE Tech. Paper 2011-01-2275.

[3] J. Leuchter, V. Refucha, Z. Krupka, and P. Bauer, "Dynamic behavior of mobile generator set with variable speed and diesel engine," in *IEEE PESC/IEEE Power Electron. Spec. Conf.*, Jun. 17–21, 2007, pp. 2287–2293.

[4] M. Duoba, H. Ng, and R. Larsen, "Characterization and comparison of two hybrid electric vehicles (HEVS)—Honda insight and Toyota Prius," presented at the Soc. Automotive Eng. Congr. Exp., Warrendale, PA, USA, 2001, SAE Tech. Paper 2001-01-1335.

[5] L. B. Lave and H. L. MacLean, "An environmental-economic evaluation of hybrid electric vehicles: Toyota's Prius vs. its conventional internal combustion engine corolla," *Transp. Res. D, Transp. Environ.*, vol. 7, no. 2, pp. 155–162, Mar. 2002.

[6] Oshkosh Defense, HEMTT A3 Diesel Electric Product Sheet, accessed 19-Nov-2013. [Online]. Available: http://www.oshkoshdefense.com/products/12/hemtt-a3-diesel-electric#lit

[7] Z. Filipi and Y. J. Kim, "Hydraulic hybrid propulsion for heavy vehicles: Combining the simulation and engine-in-the-loop techniques to maximize the fuel economy and emission benefits," *Oil Gas Sci. Technol.—Revue d'IFP Energies Nouvelles*, vol. 65, no. 1, pp. 155–178, 2010.

[8] M. Sorrentino, G. Rizzo, and I. Arsie, "Analysis of a rule-based control strategy for on-board energy management of series hybrid vehicles," *Control Eng. Pract.*, vol. 19, no. 12, pp. 1433–1441, Dec. 2011.

[9] A. Sciarretta, M. Back, and L. Guzzella, "Optimal control of parallel hybrid electric vehicles," *IEEE Trans. Control Syst. Technol.*, vol. 12, no. 3, pp. 352–363, May 2004.

[10] S. Yang, C. Qi, D. Guo, Y. Wang, and Z. Wei, "Topology optimization of a parallel hybrid electric vehicle body in white," *Appl. Mech. Mater.*, vol. 148/149, pp. 668–671, Dec. 2012.

[11] J. Liu, J. Hagena, H. Peng, and Z. S. Filipi, "Engine-in-the-loop study of the stochastic dynamic programming optimal control design for a hybrid electric HMMWV," *Int. J. Heavy Syst.*, vol. 15, no. 2–4, pp. 309–326, 2008.

[12] Y. Li and N. Kar, "Advanced design approach of power split device of plug-in hybrid electric vehicles using dynamic programming," in *Proc. IEEE Veh. Power Propulsion Conf.*, Sep. 6–9, 2011, pp. 1–6.

[13] A. Ramasamy, A. M. Hill, A. E. Hepper, A. M. J. Bull, and J. C. Clasper, "Blast mines: Physics, injury mechanisms and vehicle protection," *J. R. Army Med. Corps*, vol. 155, no. 4, pp. 258–264, Dec. 2009.

[14] A. Konev, L. Lezhnev, and I. Kolmanovsky, "Control strategy optimization for a series hybrid vehicle," presented at the Soc. Automotive Eng. World Congr., Detroit, MI, USA, 2006, SAE Tech. Paper 2006-01-0663.

[15] Y. Kim, T.-K. Lee, and Z. Filipi, "Frequency domain power distribution strategy for series hybrid electric vehicles," *SAE Int. J. Alternative Powertrains*, vol. 1, no. 1, pp. 208–218, Apr. 2012.

[16] S. Di Cairano, W. Liang, I. V. Kolmanovsky, M. L. Kuang, and A. M. Phillips, "Power smoothing energy management and its application to a series hybrid powertrain," *IEEE Trans. Control Syst. Technol.*, vol. 21, no. 6, pp. 2091–2103, Nov. 2012.

[17] S. Onori, P. Spagnol, V. Marano, Y. Guezennec, and G. Rizzoni, "A new life estimation method for lithium-ion batteries in plug-in hybrid electric vehicles applications," *Int. J. Power Electron.*, vol. 4, no. 3, pp. 302–319, 2012.

[18] S. Moura, J. Stein, and H. Fathy, "Battery-health conscious power management in plug-in hybrid electric vehicles via electrochemical modeling and stochastic control," *IEEE Trans. Control Syst. Technol.*, vol. 21, no. 3, pp. 679–694, May 2013.

[19] H. E. Perez *et al.*, "Parameterization and validation of an integrated electro-thermal LFP battery model," in *Proc. ASME Dyn. Syst. Control Conf.*, Fort Lauderdale, FL, USA, Oct. 17–19, 2012, pp. 41–50.

[20] J. R. Hagena, Z. S. Filipi, and D. N. Assanis, "Transient diesel emissions: Analysis of engine operation during a tip-in," presented at the

Soc. Automotive Eng. Congr. Exp., Detroit, MI, USA, 2006, SAE Tech. Paper 2006-01-1151.

[21] G. Ripaccioli, D. Bernardini, S. Di Cairano, A. Bemporad, and I. Kolmanovsky, "A stochastic model predictive control approach for series hybrid electric vehicle power management," in *Proc. Amer. Control Conf.*, Jun. 30–Jul. 2, 2010, pp. 5844–5849.

[22] D. Rotenberg, A. Vahidi, and I. Kolmanovsky, "Ultracapacitor assisted powertrains: Modeling, control, sizing, the impact on fuel economy," *IEEE Trans. Control Syst. Technol.*, vol. 19, no. 3, pp. 576–589, May 2011.

[23] T.-K. Lee, Y. Kim, A. Stefanopoulou, and Z. Filipi, "Hybrid electric vehicle supervisory control design reflecting estimated lithium-ion battery electrochemical dynamics," in *Proc. Amer. Control Conf.*, 2011, pp. 388–395.

[24] C.-C. Lin, H. Peng, J. Grizzle, and J.-M. Kang, "Power management strategy for a parallel hybrid electric truck," *IEEE Trans. Control Syst. Technol.*, vol. 11, no. 6, pp. 839–849, Nov. 2003.

[25] C.-C. Lin, H. Peng, and J. Grizzle, "A stochastic control strategy for hybrid electric vehicles," in *Proc. Amer. Control Conf.*, 2004, vol. 5, pp. 4710–4715.

[26] R. Johri, A. Salvi, and Z. Filipi, "Real-time transient soot and NOx virtual sensors for diesel engine using neuro-fuzzy model tree and orthogonal least squares," *Trans. ASME, J. Eng. Gas Turbines Power*, vol. 134, no. 9, pp. 092806-1–092806-9, Jul. 2012.

[27] M. Montazeri-Gh, A. Poursamad, and B. Ghalichi, "Application of genetic algorithm for optimization of control strategy in parallel hybrid electric vehicles," *J. Franklin Inst.*, vol. 343, no. 4/5, pp. 420–435, Jul./Aug. 2006.

[28] V. Paladini, T. Donateo, A. de Risi, and D. Laforgia, "Super-capacitors fuel-cell hybrid electric vehicle optimization and control strategy development," *Energy Convers. Manage.*, vol. 48, no. 11, pp. 3001–3008, Nov. 2007.

[29] Z. Wang, B. Huang, Y. Xu, and W. Li, "Optimization of series hybrid electric vehicle operational parameters by simulated annealing algorithm," in *Proc. IEEE Int. Conf. Control Autom.*, May 30–Jun. 1, 2007, pp. 1536–1541.

[30] J. Ryu, Y. Park, and M. Sunwoo, "Electric powertrain modeling of a fuel cell hybrid electric vehicle and development of a power distribution algorithm based on driving mode recognition," *J. Power Sources*, vol. 195, no. 17, pp. 5735–5748, Sep. 2010.

[31] T. Ersal *et al.*, "Development and model-based transparency analysis of an Internet-distributed hardware-in-the-loop simulation platform," *Mechatronics*, vol. 21, no. 1, pp. 22–29, Feb. 2011.

[32] T. Ersal, M. Brudnak, J. L. Stein, and H. K. Fathy, "Statistical transparency analysis in Internet-distributed hardware-in-the-loop simulation," *IEEE/ASME Trans. Mechatronics*, vol. 17, no. 2, pp. 228–238, Apr. 2012.

[33] T. Ersal, R. B. Gillespie, M. Brudnak, J. L. Stein, and H. Fathy, "Effect of coupling point selection on distortion in Internet-distributed hardware-in-the-loop simulation," *Int. J. Veh. Des.*, vol. 61, no. 1, pp. 67–85, 2013.

[34] Argonne Nat. Lab., Lemont, IL, USA, Powertrain Systems Analysis Toolkit, 2002, accessed 18-April-2014. [Online]. Available: http://www.transportation.anl.gov/modeling_simulation/PSAT/

Youngki Kim (M'14) received the B.S. and M.S. degrees from Seoul National University, Seoul, Korea, in 2001 and 2003, respectively, and the Ph.D. degree in mechanical engineering from the University of Michigan, Ann Arbor, MI, USA, in 2014.

From 2003 to 2008, he was a Research Engineer with the R&D Division, Hyundai Motor Company. He is currently a Postdoctoral Research Fellow with the Powertrain Control Laboratory, University of Michigan. His research interests include modeling and estimation of electrochemical energy storage systems and control of hybrid powertrain systems.

Ashwin Salvi received the Ph.D. degree in mechanical engineering from the University of Michigan, Ann Arbor, MI, USA, studying the thermal properties of deposit layers in exhaust gas recirculation (EGR) coolers.

He is currently a Fellow with Advanced Research Projects Agency-Energy, U.S. Department of Energy, Washington, DC, USA. His research activities during his graduate experience consisted of alternative fuel (i.e., biodiesel, jet fuel, and synthetic fuel) combustion and emissions, combustion analysis, diesel particulate and NOx emissions, fuel economy improvements and emissions reductions via hybrid architectures, engine-in-the-loop transient engine operation, hydraulic hybrid powertrain in the loop, Internet-distributed hardware in the loop, EGR cooler fouling, thermal characterization of deposit layers, and in-cylinder residual gas estimation.

Anna G. Stefanopoulou (F'09) received the Diploma in naval architecture and marine engineering from the National Technical University of Athens, Athens, Greece, in 1991 and the Ph.D. degree in electrical engineering and computer science from the University of Michigan, Ann Arbor, MI, USA, in 1996.

From 1996 to 1997, she was a Technical Specialist with Ford Motor Company. From 1998 to 2000, she was an Assistant Professor with the University of California, Santa Barbara, CA, USA. She is currently a Professor with the University of Michigan and the Director of the Automotive Research Center, Ann Arbor, which is a U.S. Army Center of Excellence in Modeling and Simulation of Ground Vehicles. She is a coauthor of a book on the control of fuel-cell power systems and is the holder of ten U.S. patents. She has 200 publications on estimation and control of internal combustion engines and electrochemical processes, such as fuel cells and batteries.

Dr. Stefanopoulou is a Fellow of the American Society of Mechanical Engineers (ASME), the Inaugural Chair of the ASME Dynamic System and Control Division Energy Systems Technical Committee, a member of the Society of Automotive Engineer Dynamic System Modeling Standards Committee, and a member of the U.S. National Academies committee on Vehicle Fuel Economy Standards. She has received five Best Paper Awards.

Tulga Ersal received the B.S.E. degree from Istanbul Technical University, Istanbul, Turkey, in 2001 and the M.S. and Ph.D. degrees from the University of Michigan, Ann Arbor, MI, USA, in 2003 and 2007, respectively, all in mechanical engineering.

He is currently an Assistant Research Scientist with the Department of Mechanical Engineering, University of Michigan. His research interests include modeling, simulation, and control of dynamic systems, with applications to energy systems, multibody dynamics, vehicle systems, and biomechanics.

Dr. Ersal is a member of the American Society of Mechanical Engineers. He received the Deans and Presidents Awards from Istanbul Technical University, the Siemens Excellence Award, and three merit fellowships from Istanbul Technical University and the University of Michigan. He also received the Semi-Plenary Paper Award at the 2012 Dynamic Systems and Control Conference.